metals

MDPI

Article

Additive Manufacturing with Superduplex Stainless Steel Wire by CMT Process

Malin Lervåg [1], Camilla Sørensen [2], Andreas Robertstad [2], Bård M. Brønstad [2], Bård Nyhus [1], Magnus Eriksson [1], Ragnhild Aune [1], Xiaobo Ren [1], Odd M. Akselsen [1] and Ivan Bunaziv [1,*]

1 Materials and Nanotechnology, SINTEF Industry, P.O. Box 4760 Torgarden, NO-7465 Trondheim, Norway; malin.lervaag@sintef.no (M.L.); Bard.Nyhus@sintef.no (B.N.); magnus.eriksson@sintef.no (M.E.); Ragnhild.Aune@sintef.no (R.A.); xiaobo.ren@sintef.no (X.R.); Odd.M.Akselsen@sintef.no (O.M.A.)

2 Department of Mechanical and Industrial Engineering, Norwegian University of Science and Technology, Richard Birkelands vei 2B, NO-7491 Trondheim, Norway; Camilla.S.S@hotmail.com (C.S.); Anrob@online.no (A.R.); bardbronstad@gmail.com (B.M.B.)

* Correspondence: ivan.bunaziv@sintef.no; Tel.: +47-457-95-269

Received: 11 January 2020; Accepted: 17 February 2020; Published: 19 February 2020

Abstract: For many years, the oil and gas industry has utilized superduplex stainless steels due to their high strength and excellent corrosion resistance. Wire arc additive manufacturing (WAAM) was used with superduplex filler wire to create walls with different heat input. Due to the multiple heating and cooling cycles during layer deposition, brittle secondary phases may form such as intermetallic sigma (σ) phase. By inspecting deposited walls within wide range of heat inputs (0.40–0.87 kJ/mm), no intermetallic phases formed due to low inter-pass temperatures used, together with the high Ni content in the applied wire. Lower mechanical properties were observed with high heat inputs due to low ferrite volume fraction, precipitation of Cr nitrides and formation of secondary austenite. The walls showed good toughness values based on both Charpy V-notch and CTOD (crack tip opening displacement) testing.

Keywords: wire arc additive manufacturing (WAAM); stainless steel; microstructure; mechanical properties; toughness

1. Introduction

Additive manufacturing (AM) technologies, commonly known as 3D printing, have been the subject of significant progress over the past decade; a comprehensive review of the process is made by DebRoy et al. [1]. AM is based on depositing single layers on the previous layers forming a complex shape with high efficiency of material utilization compared to subtractive processes such as milling. By depositing subsequent layers, previous layers are re-heated experiencing multiple liquid-solid and solid-state phase transformations. A widely used powder bed fusion (PBF) or selective laser sintering (SLS) process, where the laser or electron beam equipment is typically applied as the power source [2], may create any shape of complexity but more restricted to prototyping since the process is very slow. Wire arc additive manufacturing (WAAM) is a type of direct metal deposition (DMD) process, which utilizes filler wire and arc as heating source, enabling much higher productivity. However, some limitation exists such as low-to-medium shape complexities if small part needs to be created [3]. Moreover, WAAM is cheaper and more readily to be implemented in the industry. For AM, a limited choice of alloys is used due to prototyping with specific properties [4]. The most widely used alloy for AM is Ti-6Al-4V [1,5–12], especially concerning fatigue properties [13–15], due to wide use in medical, aircraft, aerospace and automotive industries belonging to high-value complex parts requiring only limited production volumes.

For WAAM, the cold metal transfer (CMT) process, introduced 15 years ago [16], is often used and is based on reciprocating motions of the filler wire and short-circuiting or dip transfer mode of the material [17,18]. This enables much lower heat input and reduced spatter compared to conventional pulsed arc mode. Still, the process provides respectable deposition rates.

Titanium alloys are very popular material for AM and very well understood along with austenitic stainless steels such as AISI 304 and 316 [19–25]. There are a very few studies available for duplex stainless steel (22Cr5Ni) consisting of approximately 50% ferrite and 50% austenite. It was reported [26] that the ferrite content in subsequently deposited layers is reduced along with hardness compared to the support plate. Stützer et al. [27] used a new approach for estimation of ferrite (α)/austenite (γ) balance with different wires and CMT technology and achieved a balance of 50%/50% of austenite and ferrite with good mechanical and corrosion properties.

Superduplex stainless steels are more seldom studied. These have higher content of expensive alloying elements (25Cr7Ni) for more superior corrosion resistance and, thus, more often used in the oil and gas industry where strength and corrosion are determining factors. Recently, Zhang et al. [28] showed difficulties in achieving balanced amounts of α/γ phases, where an austenite fraction increase was inevitable due to precipitation of the intragranular secondary austenite during deposition. Moreover, the presence of CrN/Cr_2N and various impurities were responsible for losses in mechanical properties.

In the present work, superduplex stainless steel wire was used for WAAM process to understand the effect of heat input on mechanical properties and to provide more experimental data and knowledge in 3D printing of this expensive steel due to its rare use. In AM of this steel grade, there is a concern of inappropriate microstructure evolution and risk of formation/precipitation of brittle intermetallic phases such as σ (sigma) [29] or χ (chi) [30,31]. They are generated at high temperatures (650–950 °C) at certain holding times, as during the reheating in AM. Other harmful phases that may form are Cr_2N (chromium nitride) and γ_2 (secondary austenite). Up to recent, σ phase formation is thought to be most detrimental since it significantly reduces the corrosion resistance, ductility and toughness [32]. The main elements for increasing the susceptibility to σ phase precipitation are Cr, Mo and Si [33]. Based on the results obtained, within the employed range of heat input, σ phase formation was suppressed but formation of Cr nitrides and secondary austenite has been documented.

2. Methodology

2.1. Materials

A 12 mm thick 2507 superduplex steel was used as support (base) plate (BM). The superduplex steel filler wire was 1.2 mm in diameter with high Ni and W content and the chemical compositions (mill certificate values) are reflected in Table 1. The BM had yield and tensile strength of 662 and 834 MPa, respectively, with a ferrite volume fraction of 48 vol.%. The wire gives typical weld metal yield (0.2% proof strength, $R_{p0.2}$) and tensile strength of 655 and 934 MPa in the as welded condition, respectively, with an impact energy of 100 J at −50 °C (mill certificate values).

Table 1. Chemical composition of selected filler wire and support plate. (Fe is balanced).

Material	C	Si	Mn	P	S	Cr	Ni	Mo	Cu	N	W
Wire	0.018	0.30	0.70	0.020	0.0010	25.0	9.5	3.7	0.60	0.23	0.6
BM	0.020	0.32	0.85	0.023	0.0003	24.8	6.6	3.7	0.16	0.26	n.a. *

* n.a. = not added.

2.2. Experimental Procedure

All layers were deposited using CMT power source (Fronius TransPuls Synergic 3200 Pipe HE). The process parameters are shown in Table 2. The arc was with DC+ polarity with an average voltage of about 14 V. The shielding gas consisted of argon with 2% CO_2 and 0.03% NO (group Z according to

ISO 14175 [34]) for arc stability, with a flow rate of 20 L/min. A schematic illustration of the deposition of walls is shown in Figure 1. The maximum inter-pass temperature was set to 100 °C. The balance of heat input and interpass temperature is critical since it affects the formation of intermetallic σ phase.

Table 2. Process parameters employed in layer deposition.

Parameter	Sample No.		
	1	2	3
No. of layers	12	11	8
Wire feed rate (mm/s)	84.7	106	106
Avg. current (A)	185	212	212
Avg. voltage (V)	14	14	14
Travel speed (mm/s)	6.4	5.5	3.4
Contact tip to work distance, CTWD (mm)	12	12	12
Heat input per layer (kJ/mm)	0.40	0.54	0.87

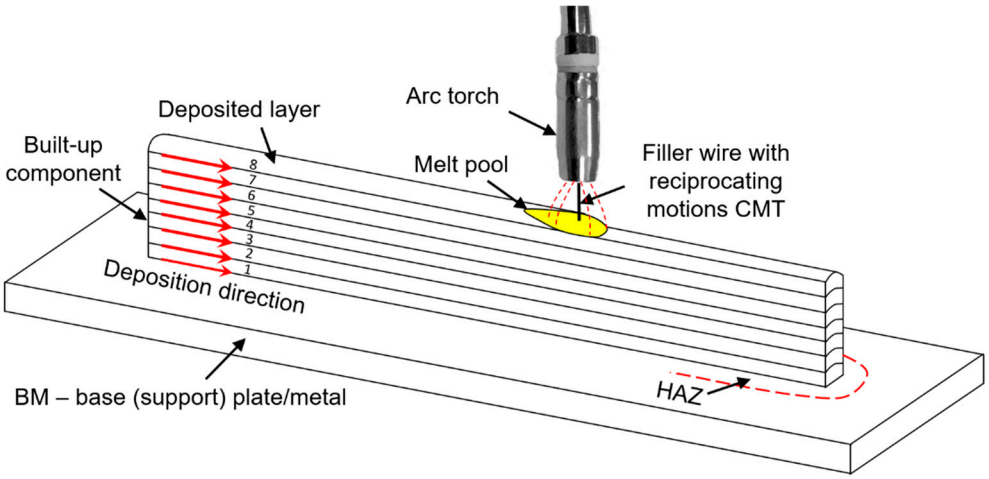

Figure 1. Schematic illustration of additive manufacturing of component.

2.3. Destructive Mechanical Testing and Analysis

Macroscopic, metallographic evaluation, tensile test, impact test and hardness evaluation were performed. Round bars for tensile testing were extracted both parallel (horizontal) and perpendicular (vertical) to the layer deposition direction, see Figure 2, having the following dimensions: 38 mm total length, 12 mm gauge length (L_0) and 4 mm diameter over the gauge length. Two parallel tests were performed. The vertical samples were "prolonged" into the base metal to achieve the length of 38 mm. The gauge area was then displaced towards the layers, providing fracture taking place in the superduplex wall.

Three parallels of sub-sized Charpy V-notch [35] samples were cut with dimensions of 5 × 10 × 55 mm^3 and subsequently machined (see Figure 2) with the notch position so that the fracture direction was perpendicular to the deposition direction. The test temperature was −20 °C. A total number of six Charpy V-notch specimens were cut from BM; three of them with sub-sized (5 × 10 × 55 mm^3), and three with full-sized (10 × 10 × 55 mm^3) dimensions, the latter one being reference toughness. According to the DNVGL-OS-F101 standard [36], values for sub-sized specimens were multiplied by a factor of two for conversion to full-sized case.

Fracture toughness CTOD (Crack Tip Opening Displacement) testing was performed at −20 °C using sub-sized SENB (Single Edge Notched Bending) $B \times 2B$ the standard rectangular specimen, using the dimensions of B = 5 mm (width) and $2B$ = 10 mm (height, sample thickness). The notch placement was the same as Charpy, but with a geometry of $a/t = 0.5$ (a is the length of notch and fatigue

pre-crack, $W = 2B$ is thickness). The notch was electro discharged to a depth of 4 mm followed by fatigue pre-cracking up to a depth of 4.8 mm.

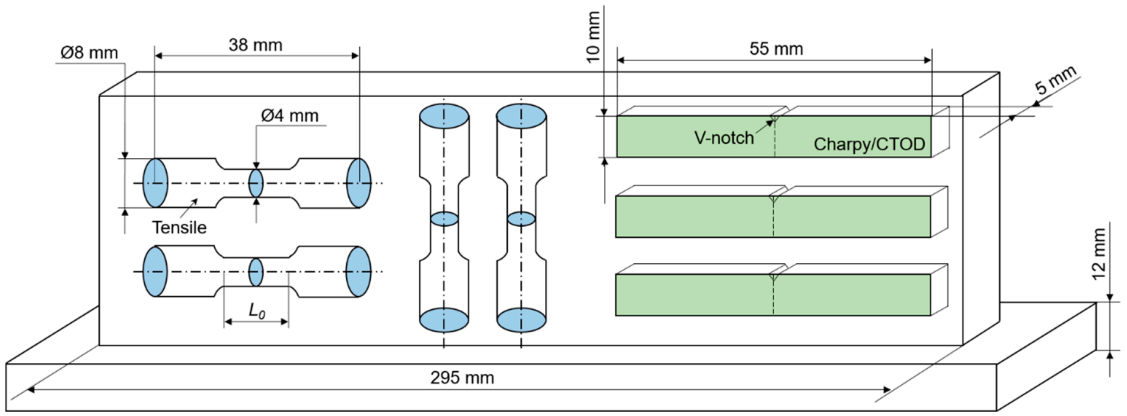

Figure 2. Mechanical testing of additively manufactured walls. Horizontal tensile samples to the left, vertical tensile specimens in the middle and Charpy V and CTOD (crack tip opening displacement) samples to the right. The latter two specimen types have different notches.

A transversal cross-section of the wall for each sample was extracted for macro- and microscopic inspection, the ZwickRoell ZHV unit was used for Vickers hardness measurements (HV_{10}, with 10 kg force). The microstructure examination of walls was performed in light microscope. For the ferrite volume fraction assessment, a point counting technique was used for the first, middle and last bead, including heat affected zone (HAZ) and BM. A total number of 13 fields was included per position in the wall for ferrite counting. In these fields, a grid system with 100 points was used. The magnification was ×1000. The ISO 9042 standard [37] recommends 30 grids to achieve a statistical reliability. However, the standard also reports a multiplication factor if less than 30 grids are used. In the present case with 13 grids, the factor is 2.16 for calculating the 95% confidence interval.

To obtain good contrast between austenite and ferrite, the specimens were electrolytically etched in 40% NaOH, operating at a voltage of 7 V for 15 s, followed by a light polish for 10 s. For identification of the Cr nitrides, the specimens were re-prepared and electrolytically etched in 10% oxalic acid, $C_2H_2O_4$, for 10 s, operating at room temperature with 6 V. Finally, the samples were etched in 10% oxalic acid for 3 s at 6 V, then in 60% nitric acid for 15 s at 1 V to identify the σ phase.

3. Results and Discussions

3.1. Structure of Additively Manufactured Walls

The macrosections of additively deposited walls are represented in Figure 3. The average widths of the deposited walls were 7.5 mm (sample 1, 0.40 kJ/mm), 8.5 mm (sample 2, 0.54 kJ/mm) and 11.0 mm (sample 3, 0.87 kJ/mm). The average layer height for the three different walls was 2.4, 2.8 and 3.4 mm for samples 1–3, respectively, which is consistent with the heat input variation. Neither pores nor cracking were visible, which means that the employed parameters are appropriate for production of AM walls.

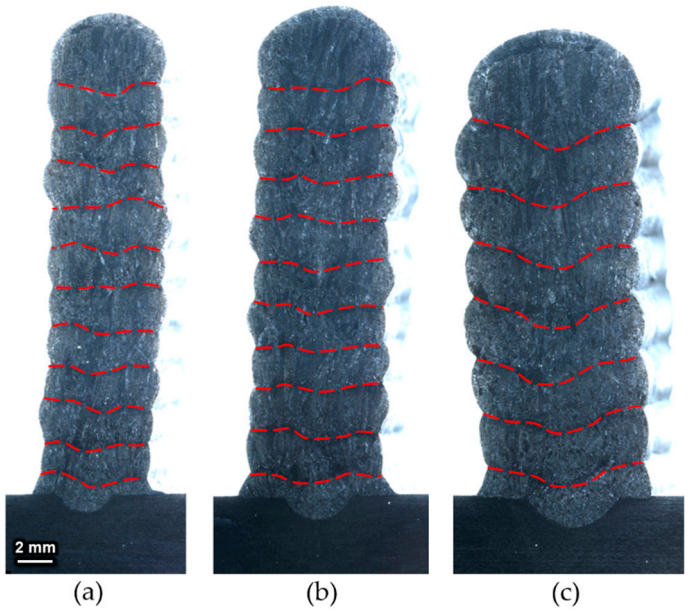

Figure 3. Macrosections of additively manufactured walls: (**a**) 0.40 kJ/mm, (**b**) 0.54 kJ/mm and (**c**) 0.87 kJ/mm. The dashed red lines indicate boundaries between deposited layers.

3.2. Tensile Data

The individual stress-strain curves are shown in Figure 4. There is a minor scatter found between the two parallels, primarily occurring for the reduction in area. This is expected due to the inhomogeneity of microstructures throughout the layers (later shown in Sections 3.6 and 3.9).

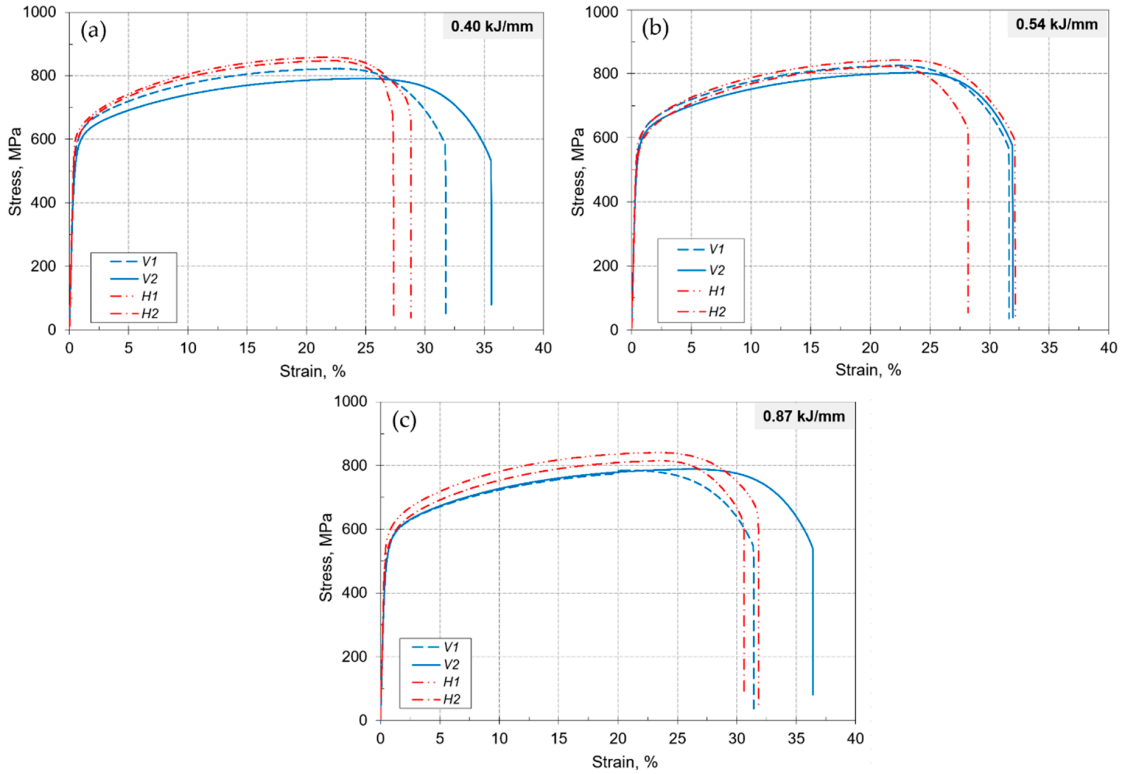

Figure 4. Stress strain curves of samples with heat inputs of (**a**) 0.40 kJ/mm, (**b**) 0.54 kJ/mm and (**c**) 0.87 kJ/mm. *H1*/*H2* are horizontal and *V1*/*V2* are vertical samples.

One observation is that the WAAM deposited layer gave in most cases lower strength than that of the support plate, and the strength values fall below the typical values indicated in the wire datasheet (Section 2.1). This may be linked to the small size of the tensile specimens used in the present case. More important is that horizontal and vertical samples had different strength and ductility; the strength of horizontal specimens tends to be slightly higher than those of the vertical ones. This is probably linked to the fact that vertical samples represent more extensive reheating effects.

According to data presented in Figure 5, yield and tensile strength are reduced with an increase of heat input. The slope of the linear trend is larger for the yield ($R_{p0.2}$) than for the tensile strength (R_m). For the highest heat input, the yield strength was reduced by 160 and 100 MPa for vertical and horizontal samples, respectively, when comparison is made with the BM. The loss in tensile strength was much smaller (< 20 MPa). However, when compared with the tensile strength of the wire (934 MPa), the loss in the ultimate tensile strength is at the same level as the yield point. By contrast to strength, the ductility showed an opposite trend as shown in Figure 6.

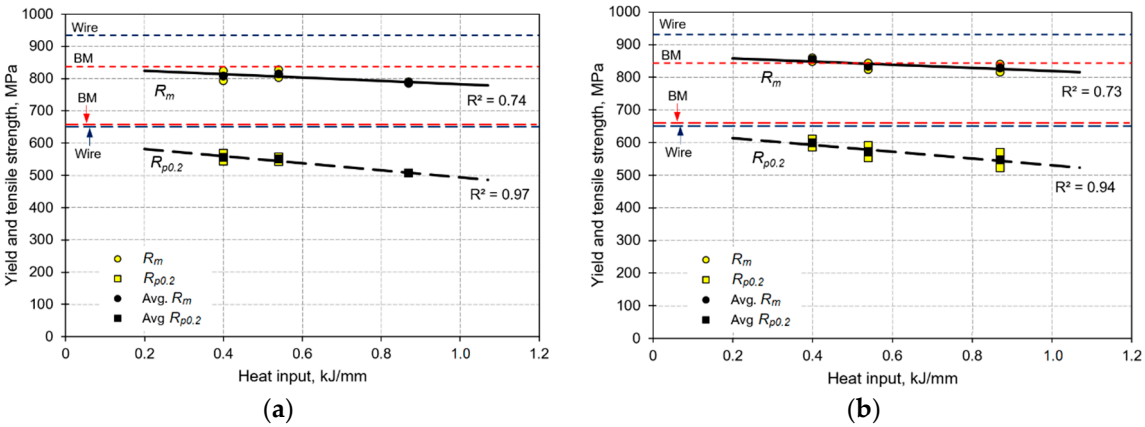

Figure 5. Effect of heat input on yield ($R_{p0.2}$) and tensile (R_m) strength for (**a**) vertical samples and (**b**) horizontal samples.

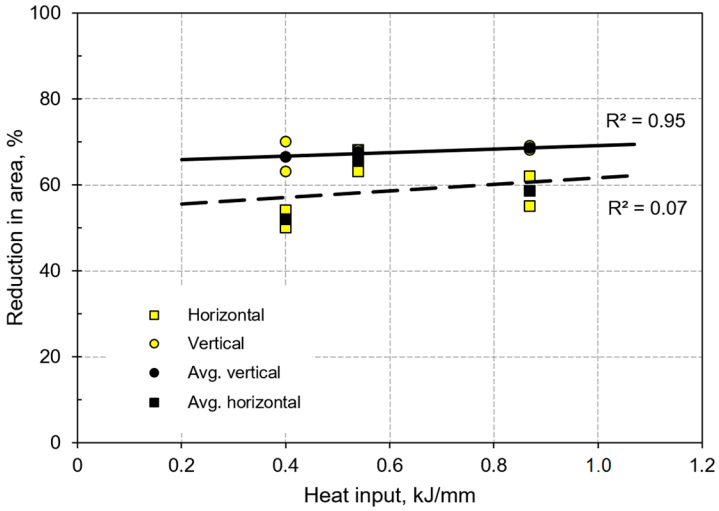

Figure 6. Effect of heat input on reduction in area.

3.3. Hardness

Higher hardness was developed in the HAZ of the base metal, where maximum 271 HV was measured for sample 1 (0.40 kJ/mm), and with slightly lower hardness in deposited layers, see Figure 7. The hardness for the deposited layers and the HAZ satisfies most of requirement set in current offshore standards (< 300 HV). However, an exception is the requirements for sour service, usually set to

248 HV according to ISO 15156 [38,39]. The maximum hardness in the HAZ and weld metal (WM) can be further reduced through an increase in heat input. Based on the linear trendlines (see Figure 7), a heat input of 1.0 kJ/mm is required to achieve 248 HV in the HAZ, which is still below a critical heat input for sigma (σ) phase formation. The problem here is that the heat input should not be increased further since it may cause formation of brittle phases in the HAZ. By application of superduplex steel wire, both WM and the HAZ can be more sensitive to formation of σ and χ phases due to the higher ratio between ferrite (ferrite stabilizing elements are Cr, Mo, Si) and austenite stabilizers (austenite stabilizing elements are Ni, Mn, Cu, N) than contained in conventional 2205 duplex stainless steels.

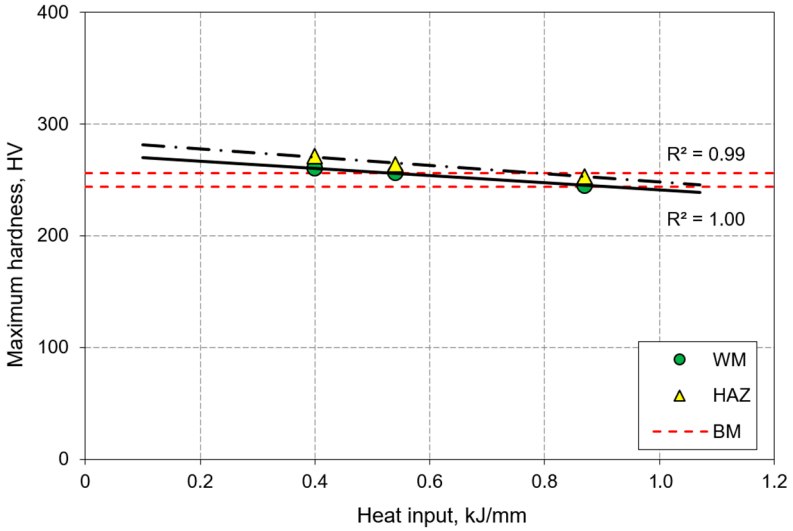

Figure 7. Effect of heat input on hardness in deposited layers (WM) and heat affected zone (HAZ).

3.4. Toughness Results

The effect of heat input on the Charpy V-notch toughness is shown in Figure 8. The results for sub-sized samples are converted to full sized samples by multiplication by a factor of two (sub-sized samples have only 50% of the cross section of full-sized ones). It is found that the toughness of deposited layers is only 30%–35% compared to the BM. The Charpy V values are almost independent of the employed heat input. Only a slight reduction in toughness occurs when increasing the heat input from 0.40 to 0.87 kJ/mm. This is possibly related to the coarsening of the microstructure when the heat input is increased. Accordingly, it is reasonable to assume that no harmful intermetallics have been formed (to be discussed later). With the formation of σ, a much sharper fall in toughness would be expected.

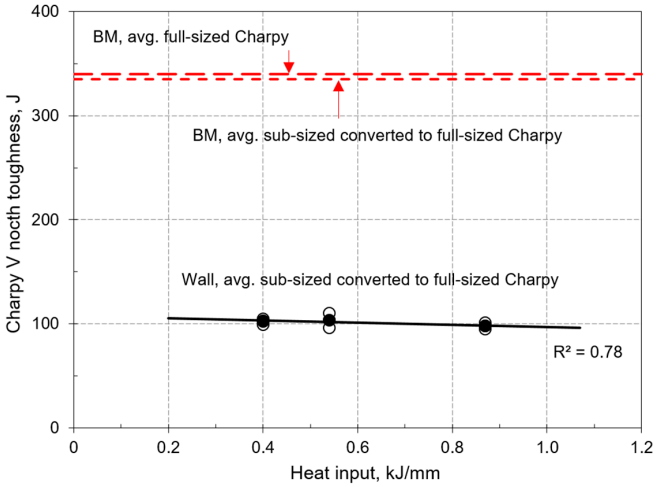

Figure 8. Charpy V-notch toughness of walls and base metal.

The fracture toughness results (CTOD test) are shown in Figure 9. The CTOD level is around 0.3 mm, although a small enhancement in the average value is found when the heat input is increased. In general, a value of 0.3 mm provides acceptable toughness values based on DNVGL-OS-C401 [40] the critical value is 0.15 mm.

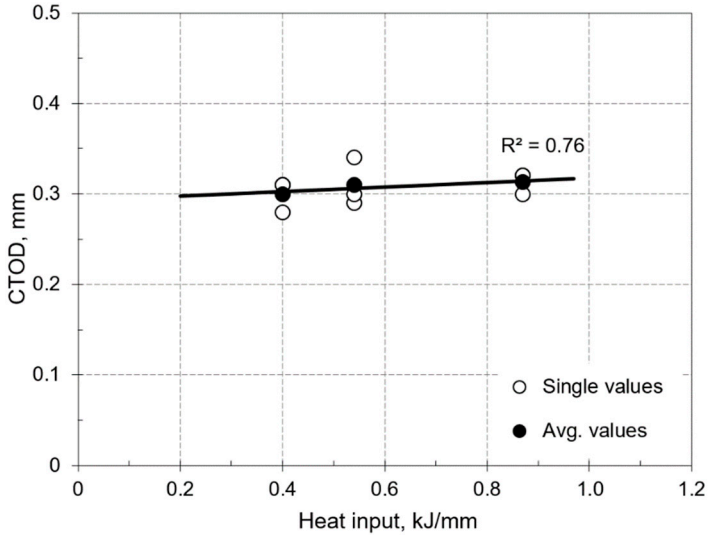

Figure 9. CTOD fracture toughness of walls.

3.5. Solidification

Stainless steel may solidify in different modes according to their chemical composition. In addition, the cooling rate may induce a shift in solidification [41]. In austenitic stainless steels, a three-phase reaction region exists ($Liquid \rightarrow \gamma + \delta$), which can be either eutectic or peritectic for compositions beyond 15 wt.% Cr and 10 wt.% Ni according to the Fe-Cr-Ni ternary phase diagram [42,43]. Here, δ means the high temperature ferrite and used according to literature. Consequently, the solidification microstructure, depending on both composition and cooling rate, may become more complex due to the three-phase reaction. Depending on the Cr_{eq}/Ni_{eq} ratio, stainless steel can be solidified with four different solidification modes [44,45], i.e., ferrite mode, ferrite-austenite mode, austenite-ferrite mode and austenite mode (here *Liq* means—liquid phase of the material):

$$F \text{ mode: } Liq \rightarrow Liq + \delta \rightarrow \delta \rightarrow \delta + \gamma \qquad \text{for } Cr_{eq}/Ni_{eq} > 2.0 \tag{1a}$$

$$FA \text{ mode: } Liq \rightarrow Liq + \delta \rightarrow Liq + \delta + \gamma \rightarrow \delta + \gamma \rightarrow \gamma \qquad \text{for } 1.5 < Cr_{eq}/Ni_{eq} < 2.0 \tag{1b}$$

$$AF \text{ mode: } Liq \rightarrow Liq + \gamma \rightarrow Liq + \delta + \gamma \rightarrow \gamma + \delta \rightarrow \gamma \qquad \text{for } 1.37 < Cr_{eq}/Ni_{eq} < 1.5 \tag{1c}$$

$$A \text{ mode: } Liq \rightarrow Liq + \gamma \rightarrow \gamma \qquad \text{for } Cr_{eq}/Ni_{eq} < 1.37 \tag{1d}$$

The existence area of these solidification regimes is outlined in Figure 10. The values of Cr_{eq} and Ni_{eq} are calculated from Equation (2) below (elements in wt.%), taken from the Welding Research Council 1992 diagram (WRC-1992):

$$Cr_{eq} = \text{Cr} + \text{Mo} + 0.7\text{Nb} \tag{2a}$$

$$Ni_{eq} = \text{Ni} + 35\text{C} + 20\text{N} + 0.25\text{Cu} \tag{2b}$$

The Cr and Ni equivalents of the examined superduplex steel wire are 28.7 and 14.9, respectively, which gives a ratio of 1.9. This is indicated in Figure 10 as the red circle marker, which falls close to the ferrite line. Therefore, it is implied that a primary ferritic or mixed mode solidification may

occur for the current deposited layers. Figure 10 represents the Welding Research Council WRC-1992 diagram [46] for Cr_{eq} from 17 to 31 and Ni_{eq} from 9 to 18.

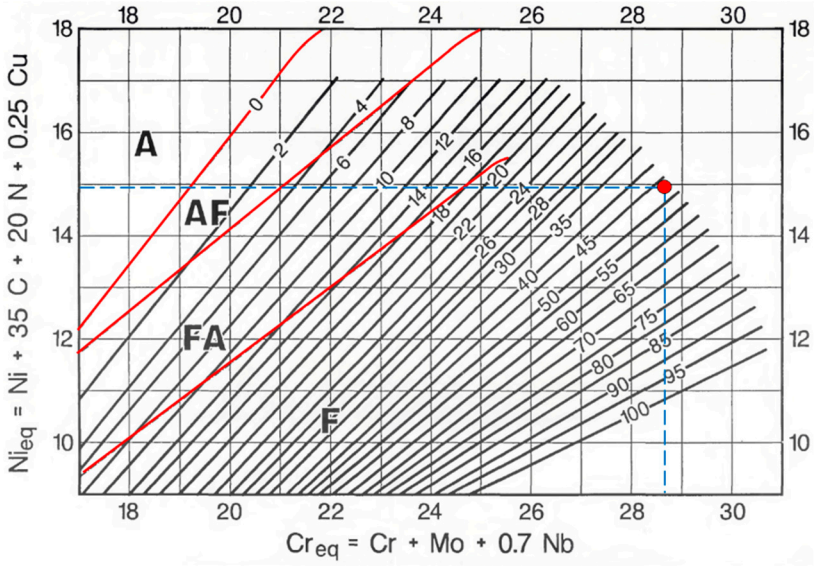

Figure 10. Nomenclature of solidification modes in stainless steels. Adapted from [46]. The wire composition is represented by the red circle marker based on the Cr and Ni equivalents adopted by WRC-1992 (Equation (2)).

The metallographic investigation demonstrated that the layers solidify by epitaxial nucleation and growth (Figure 11), which means that the solidifying grains nucleate at the grains located at the fusion boundary. Due to the high alloying level and high thermal gradient because of poor heat conduction capacity, a planar solidification front may not be stable, and the primary solidification mode is cellular-dendritic. Here, only ferrite with a crystallographic preferential growth orientation relationship aligned with the heat flow direction will continue to grow. This growth will cease when the preferred ferrite growth direction reaches a certain deviation from the heat flow direction. Then, successive nucleation of new ferrite will take place with subsequent growth of those grains with their preferred growth direction nearly parallel with the heat flow direction.

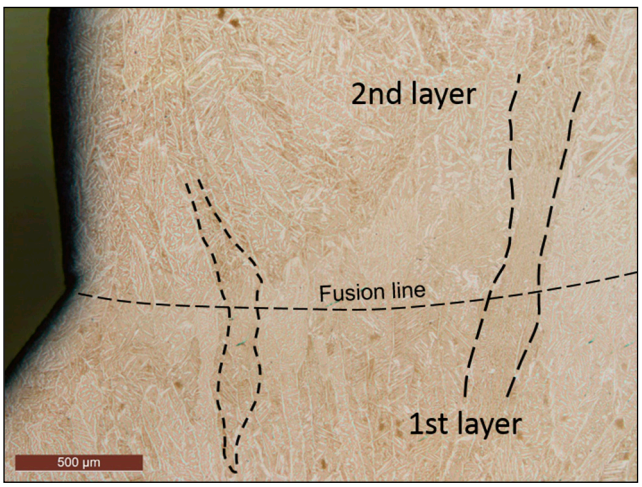

Figure 11. Micrographs with indications of epitaxial solidification (one example is shown inside black dotted lines); between first and second build layer (0.87 kJ/mm).

3.6. Ferrite Content

As stated previously (Section 2.1), the BM has 48 vol.% of ferrite and 52 vol.% of austenite balance. According to the data presented in Figure 12, the ferrite volume fraction in the walls is significantly lower (15–27 vol.%) than that of the BM. Minor variations were found between the different layers. However, the low ferrite fraction observed in the present study is strictly outside the target level of 30–65% for weld metals [36] and needs procedure qualification testing (mechanical and corrosion) prior to use in the oil and gas industry.

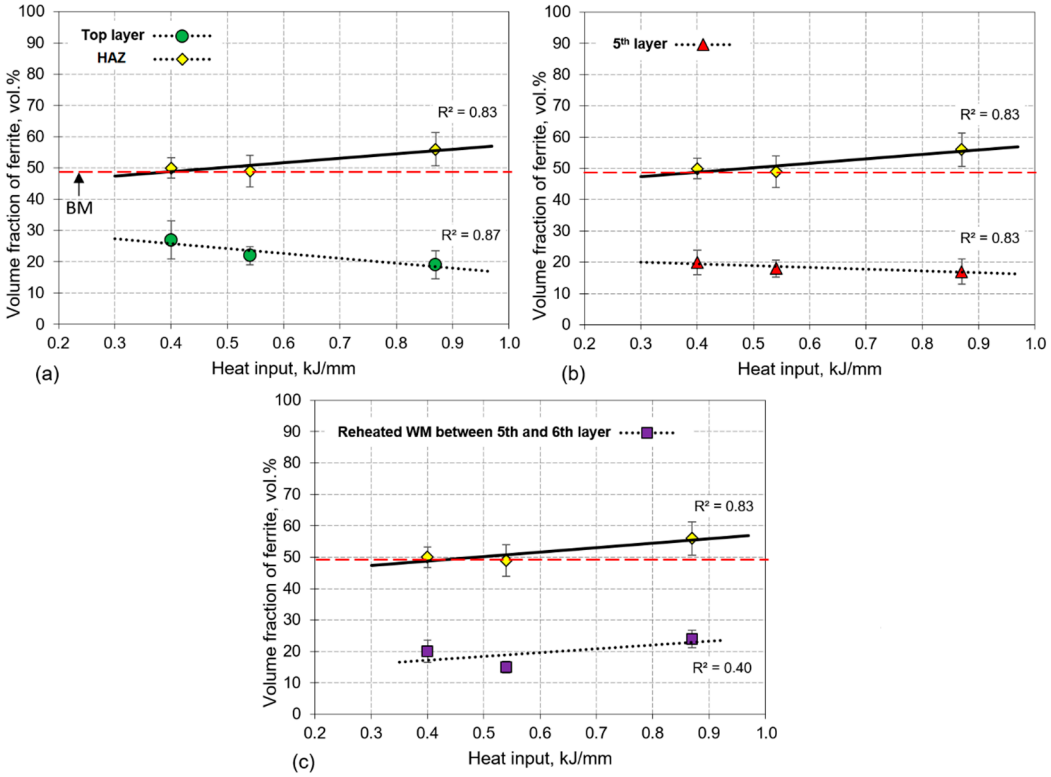

Figure 12. Effect of heat input on volume fraction of ferrite in different areas of deposited walls: (**a**) WM of top layer, (**b**) WM between 5th and 6th layer, (**c**) WM of 5th layer. The dashed red lines represent volume fraction of ferrite in the BM (48 vol.%).

This observation concerning low ferrite volume fraction is caused by the selected filler wire, promoting more austenite due to the high nickel content (9.5 wt.% Ni). This is in fact almost 3% higher than the BM (6.6 wt.% Ni). In principle, overalloying with Ni should provide a better balance of α/γ, approaching a 50%/50% distribution between the phases [47]. Thus, the low ferrite content may also arise from too slow cooling rates. Slower cooling will promote austenite formation, which is softer than the ferrite. The low ferrite fraction found in the walls may explain the lower strength compared with the base metal level. In the HAZ of the base metal, the ferrite content was similar to the BM volume fraction (49–56 vol.%) and weakly dependent on heat input range used within this study.

On reheating of as solidified metal, inevitably taking place in layer manufacturing using arc as heat source, the microstructure will depend on the temperature which is reached. When reheating to high temperature, full ferritization may occur with almost instantaneous growth of ferrite. On cooling, the ferrite may transform back to austenite of different morphologies, depending on the cooling rates. At lower temperatures, full ferritization may not take place and the austenite-to-ferrite transformation may only be partial. As a result, the final microstructure contains both transformed and untransformed ferrite, and the transformed ferrite may revert to austenite on cooling [48]. This re-transformed austenite is called secondary austenite (γ_2).

The microstructures shown in Figure 13 represent the top layer and consist of ferrite grains with extensive austenite nucleation and growth, revealing both elongated austenite grains and Widmanstätten austenite sideplates (WAS). The morphology and size of the austenite phase may influence the component properties. An example is the influence on pitting properties [49]. In reheated areas of the walls, secondary austenite is formed (Section 3.8), which is known to be harmful to corrosion resistance [50,51]. Due to the higher alloying level of superduplex stainless steels, the ferrite content will be lower than in similar layer manufacturing of 2205 or 2304 duplex stainless steel. This is particularly the case in the HAZ of BM. In the present work, this region contained 50–56 vol.% of ferrite, while in the HAZ of 2205 there is typically 80–90 vol.% ferrite [52]. A typical microstructure developed as found in Figure 14, consisting of large ferrite grains with allotriomorphic austenite along the grain boundaries including some WAS. In addition, extensive precipitation of Cr nitrides is observed (Section 3.7).

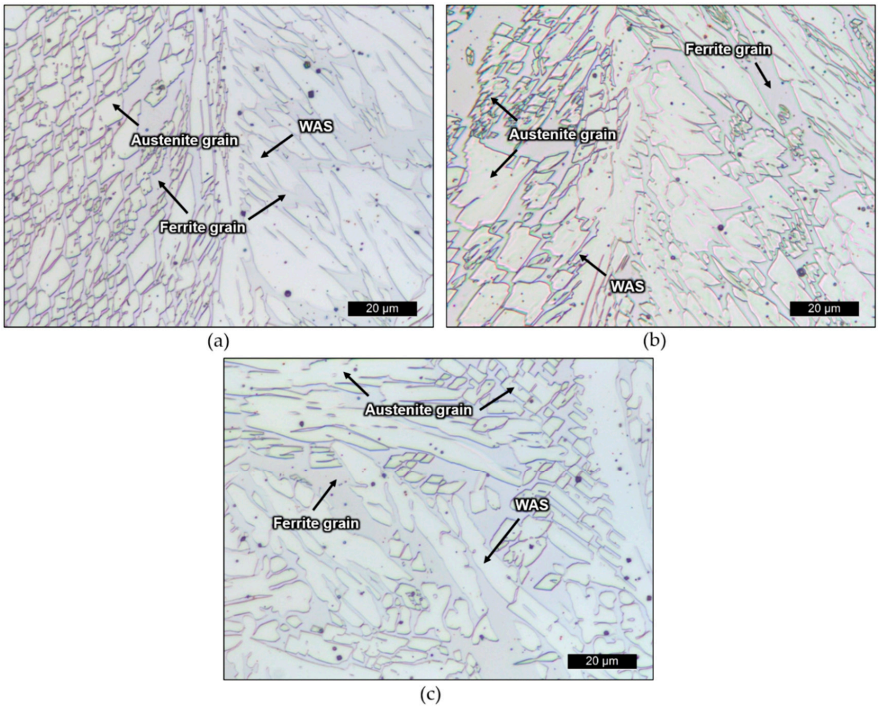

Figure 13. Microstructure in top layer in; (**a**) Sample No. 1 (0.40 kJ/mm), (**b**) Sample No. 2 (0.54 kJ/mm) and (**c**) Sample No. 3 (0.87 kJ/mm). WAS—Widmanstätten austenite side-plate.

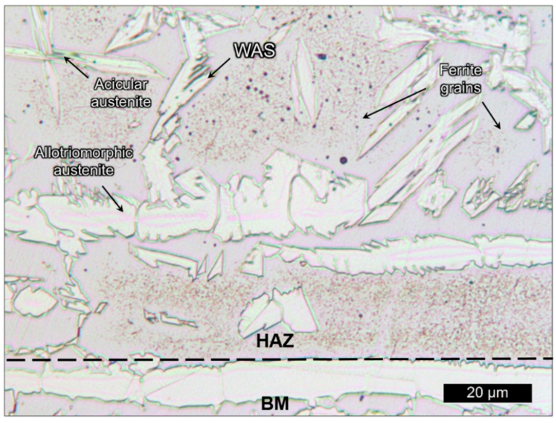

Figure 14. Microstructure in heat-affected zone. WAS—Widmanstätten austenite side-plate. The dashed black line represents the boundary between the HAZ and the unaffected BM.

3.7. Chromium Nitrides

In the HAZ of the BM, there is clearly visible precipitation of Cr nitrides, as shown in Figure 15. In comparison to the HAZ, no Cr nitrides were found in the built walls. These nitrides form inside ferrite grains during cooling (from 1250 to 1100 °C [53]). The precipitation is inhomogeneous since nitride-free areas are also found; most of them are closer to the austenitic grains. Two nitride morphologies have been previously reported found [53,54], Cr_2N and CrN, both occur as intragranular precipitates. The metastable CrN was first observed by Hertzman et al. [55] in duplex 2205 steel on rapid cooling from solution annealing at 1350 °C. Nitrogen is mainly partitioned to austenite due to limited solubility in ferrite. However, the nitrogen content in ferrite increases with increasing temperature during the heating leg of the first layer in WAAM. Therefore, nitride precipitates have propensity to form during rapid cooling from high temperatures as ferrite is supersaturated with nitrogen [54,56]. The extent of partitioning and diffusion of nitrogen in these steels will depend on the austenite spacing. With finer grain structure, and smaller austenite spacing, nitrogen may diffuse into austenite and nitride precipitates will be more homogeneously distributed inside ferrite grains [57]. Pettersson et al. [58] found primarily Cr_2N nitrides in the interior of ferrite grains. By an increase in the cooling rate and/or increase in the austenite spacing, the formation of nitrides was clearly promoted. This resulted in precipitation within a higher fraction of the ferrite grains. Larger nitride particles were also found. Furthermore, they observed formation of the metastable CrN which was induced by higher cooling rates. Due to the rapid cooling linked with the low heat input in the present study, it is reasonable to assume that CrN precipitates have formed. A confirmation of this point requires transmission electron microscopy. Cr nitrides were not found in the built wall due to the low ferrite content. The toughness seems to be unaffected by nitrides [58,59].

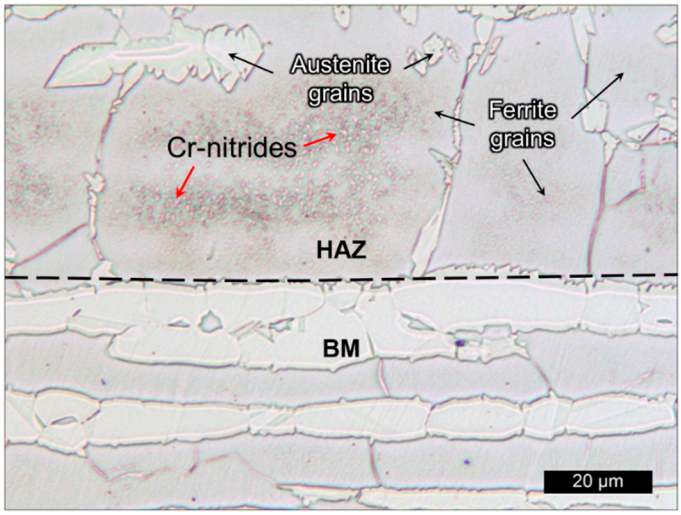

Figure 15. Cr nitrides in ferrite in HAZ. The dashed black line represents the boundary between the HAZ and the unaffected BM.

3.8. Secondary Austenite

In production of duplex stainless steels, the important target is to obtain microstructure with almost equal amount of ferrite and austenite. During WAAM, reheating will take place and the austenite transforms to ferrite at high peak temperature; depending on the alloy this transformation can be completed before the alloy is melted. On subsequent rapid cooling, austenite re-transformation will be partially suppressed giving high volume fraction of metastable ferrite. By reheating this metastable microstructure above ~800 °C, the microstructure is affected by the dissolution of the intragranular nitrides and the formation of secondary austenite (γ_2) [60]. The austenite formation occurs at α/γ interfaces, as well as intragranularly in the ferrite, as shown by the micrograph contained in Figure 16.

This observation is consistent with previous findings in the literature [61]. This kind of precipitation is possibly linked to dislocations or substructures. Moreover, secondary austenite is also reported to form on Cr_2N due to a Cr depletion from the surroundings [60]. Secondary austenite is reported to improve toughness [62], while it has been proposed that the chemical composition of γ_2 compromises the corrosion resistance [50,51]. In layer manufacturing, redistribution of alloying elements can occur due to formation of nitrides or by excessive precipitation of γ_2. The kinetic factors that can change the chemical composition of different phases may lead to local susceptibility to pitting and localized corrosion [63].

3.9. Intermetallic Phases

Numerous types of intermetallic phases, as well as carbide precipitates (common ones are $M_{23}C_6$ and/or M_7C_6), may form in superduplex stainless steels. Fast heating and cooling rates together with large temperature gradients are responsible for the eutectoid decomposition of ferrite [51,64–66]. Some of the possible reactions are:

$$\delta \rightarrow \delta + \gamma + \gamma_2 \quad (3a)$$

$$\delta \rightarrow \sigma + \gamma_2 \quad (3b)$$

$$\delta \rightarrow M_{23}C_6 + \gamma_2 \quad (3c)$$

$$\delta \rightarrow M_7C_6 + \gamma_2 \quad (3d)$$

As already discussed, Cr nitrides and secondary austenite has been observed in the present study in the HAZ and the deposited layers, respectively. The sigma phase which forms in the temperature range between 650 and 950 °C has not been found with light microscopy using etchants that reveal the σ phase. The sigma phase has a large tetragonal unit cell of 32 atoms and has therefore a sluggish transformation nature [67]. However, its formation can be promoted when cooling conditions and microstructural variations favor nucleation. Alloying additions (Cr, Mo and W) can accelerate the formation of σ phase by enlarging its field of stability. In WAAM of any duplex steels, extra attention must be considered in balancing heat input and interpass temperature due to reheating by subsequent layers to avoid formation of intermetallic phases due to their negative effect on toughness and corrosion. In the case of superduplex steel, the C-curves for precipitation of carbides, Cr nitrides and intermetallics are moved to the left towards shorter times. This will require faster cooling (lower heat input) than for conventional 2304 or 2205 duplex steels.

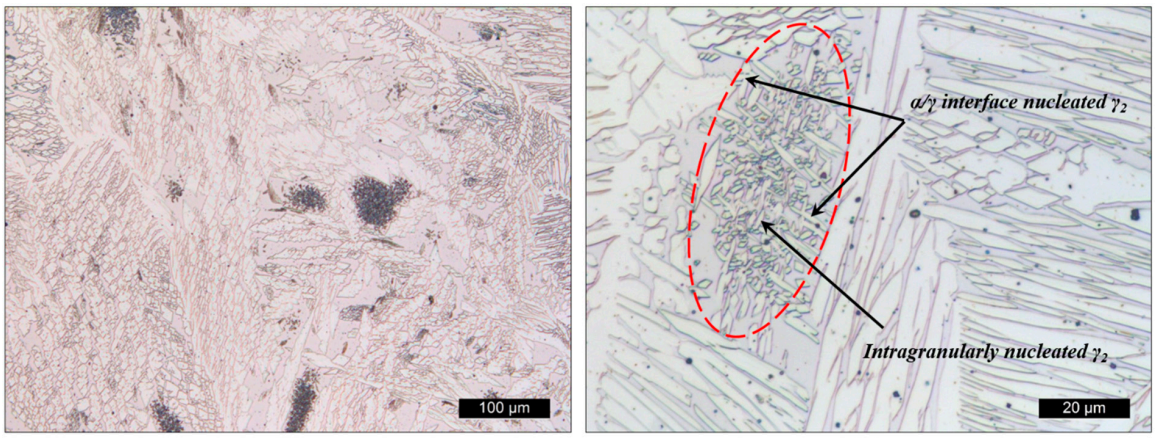

Figure 16. Secondary austenite formed in the ferrite, (**a**) overview with dark islands of γ_2, and (**b**) close-up with γ_2 inside the dotted red ellipse. Arrows point at different nucleation sites.

4. Conclusions

Based on experimental studies, addressing wire arc additive manufacturing with superduplex stainless steel wire, the following conclusions can be drawn:

- No significant weld defects were found for any of the process parameters employed.
- The measured yield strength was found to be 100–160 MPa lower than that of the base metal, depending on specimen orientation. Vertical samples had the lowest strength, which is consistent with the multiple reheating of the layers.
- The notch toughness of the walls was satisfactory, i.e., around 100 J at −20 °C. However, the level is only 30% of the base metal toughness.
- The deposited walls had low ferrite content (15–27 vol.%) due to overalloying with nickel which may explain the lower yield strength of the walls when compared to the base metal.
- Precipitation of Cr nitrides was found in the heat affected zone between the first layer and the base metal.
- Secondary austenite formation occurred in the reheated areas of the layers.
- No intermetallic phases were found within selected heat inputs.
- The deposited walls showed that WAAM of superduplex stainless steel requires adjustments in the layer deposition procedure to achieve a proper ferrite to austenite balance. Since too high austenite has been formed in the present study, faster cooling rates will be necessary through adjustments of component design, heat input and shielding gas.

Author Contributions: Methodology, O.M.A. and M.L.; experimental testing, M.L., C.S., A.R., and B.M.B.; validation, M.L., B.M.B., O.M.A., and X.R.; formal analysis, M.L., O.M.A. and I.B.; investigation, O.M.A., M.L., X.R. and I.B.; resources, M.L.; data curation, O.M.A., X.R. and I.B.; writing—original draft preparation, M.L., O.M.A. and I.B.; writing—review and editing, O.M.A., B.N., M.E., and I.B.; visualization, O.M.A. and I.B.; supervision, X.R., O.M.A., B.N., R.A., M.E., and I.B.; project administration, X.R., M.E., and O.M.A.; funding acquisition, M.E., O.M.A., and X.R. All authors have read and agreed to the published version of the manuscript.

Funding: This research was funded by the Norwegian Research Council (Contract No. 281927/E30) and the industry companies Equinor, Westad, Nordic Additive Manufacturing (NAM) and Vitec.

Conflicts of Interest: The authors declare no conflicts of interest.

References

1. DebRoy, T.; Wei, H.L.; Zuback, J.S.; Mukherjee, T.; Elmer, J.W.; Milewski, J.O.; Beese, A.M.; Wilson-Heid, A.; De, A.; Zhang, W. Additive manufacturing of metallic Components—Process, structure and properties. *Prog. Mater. Sci.* **2018**, *92*, 112–224. [CrossRef]
2. Ding, D.; Pan, Z.; Cuiuri, D.; Li, H. Wire-feed additive manufacturing of metal components: Technologies, developments and future interests. *Int. J. Adv. Manuf. Technol.* **2015**, *81*, 465–481. [CrossRef]
3. Oliveira, J.P.; Santos, T.G.; Miranda, R.M. Revisiting fundamental welding concepts to improve additive manufacturing: From theory to practice. *Prog. Mater. Sci.* **2020**, *107*, 100590. [CrossRef]
4. Frazier, W.E. Metal Additive Manufacturing: A Review. *J. Mater. Eng. Perform.* **2014**, *23*, 1917–1928. [CrossRef]
5. Waryoba, D.R.; Keist, J.S.; Ranger, C.; Palmer, T.A. Microtexture in additively manufactured Ti-6Al-4V fabricated using directed energy deposition. *Mater. Sci. Eng. A* **2018**, *734*, 149–163. [CrossRef]
6. Hemmasian Ettefagh, A.; Zeng, C.; Guo, S.; Raush, J. Corrosion behavior of additively manufactured Ti-6Al-4V parts and the effect of post annealing. *Addit. Manuf.* **2019**, *28*, 252–258. [CrossRef]
7. Sabban, R.; Bahl, S.; Chatterjee, K.; Suwas, S. Globularization using heat treatment in additively manufactured Ti-6Al-4V for high strength and toughness. *Acta Mater.* **2019**, *162*, 239–254. [CrossRef]
8. Wu, B.; Pan, Z.; Li, S.; Cuiuri, D.; Ding, D.; Li, H. The anisotropic corrosion behaviour of wire arc additive manufactured Ti-6Al-4V alloy in 3.5% NaCl solution. *Corros. Sci.* **2018**, *137*, 176–183. [CrossRef]
9. Strantza, M.; Vrancken, B.; Prime, M.B.; Truman, C.E.; Rombouts, M.; Brown, D.W.; Guillaume, P.; Van Hemelrijck, D. Directional and oscillating residual stress on the mesoscale in additively manufactured Ti-6Al-4V. *Acta Mater.* **2019**, *168*, 299–308. [CrossRef]

10. Gorji, M.B.; Tancogne-Dejean, T.; Mohr, D. Heterogeneous random medium plasticity and fracture model of additively-manufactured Ti-6Al-4V. *Acta Mater.* **2018**, *148*, 442–455. [CrossRef]
11. Bermingham, M.J.; Kent, D.; Zhan, H.; StJohn, D.H.; Dargusch, M.S. Controlling the microstructure and properties of wire arc additive manufactured Ti–6Al–4V with trace boron additions. *Acta Mater.* **2015**, *91*, 289–303. [CrossRef]
12. Carroll, B.E.; Palmer, T.A.; Beese, A.M. Anisotropic tensile behavior of Ti–6Al–4V components fabricated with directed energy deposition additive manufacturing. *Acta Mater.* **2015**, *87*, 309–320. [CrossRef]
13. Ren, D.; Li, S.; Wang, H.; Hou, W.; Hao, Y.; Jin, W.; Yang, R.; Misra, R.D.K.; Murr, L.E. Fatigue behavior of Ti-6Al-4V cellular structures fabricated by additive manufacturing technique. *J. Mater. Sci. Technol.* **2019**, *35*, 285–294. [CrossRef]
14. Wilson-Heid, A.E.; Beese, A.M. Fracture of laser powder bed fusion additively manufactured Ti–6Al–4V under multiaxial loading: Calibration and comparison of fracture models. *Mater. Sci. Eng. A* **2019**, *761*, 137967. [CrossRef]
15. Choi, Y.; Lee, D.-G. Correlation between surface tension and fatigue properties of Ti-6Al-4V alloy fabricated by EBM additive manufacturing. *Appl. Surf. Sci.* **2019**, *481*, 741–746. [CrossRef]
16. Schörghuber, M. Inventor Cold-Metal-Transfer Welding Process and Welding Installation. Patent WO 2006/125234 A1, 18 May 2006.
17. Pickin, C.G.; Williams, S.W.; Lunt, M. Characterisation of the cold metal transfer (CMT) process and its application for low dilution cladding. *J. Mater. Process. Technol.* **2011**, *211*, 496–502. [CrossRef]
18. Chen, M.; Zhang, D.; Wu, C. Current waveform effects on CMT welding of mild steel. *J. Mater. Process. Technol.* **2017**, *243*, 395–404. [CrossRef]
19. Tolosa, I.; Garciandía, F.; Zubiri, F.; Zapirain, F.; Esnaola, A. Study of mechanical properties of AISI 316 stainless steel processed by "selective laser melting", following different manufacturing strategies. *Int. J. Adv. Manuf. Technol.* **2010**, *51*, 639–647. [CrossRef]
20. Yasa, E.; Kruth, J.P. Microstructural investigation of Selective Laser Melting 316L stainless steel parts exposed to laser re-melting. *Procedia Eng.* **2011**, *19*, 389–395. [CrossRef]
21. de Lima, M.S.F.; Sankaré, S. Microstructure and mechanical behavior of laser additive manufactured AISI 316 stainless steel stringers. *Mater. Des.* **2014**, *55*, 526–532. [CrossRef]
22. Wang, Z.; Palmer, T.A.; Beese, A.M. Effect of processing parameters on microstructure and tensile properties of austenitic stainless steel 304L made by directed energy deposition additive manufacturing. *Acta Mater.* **2016**, *110*, 226–235. [CrossRef]
23. Wang, L.; Xue, J.; Wang, Q. Correlation between arc mode, microstructure, and mechanical properties during wire arc additive manufacturing of 316L stainless steel. *Mater. Sci. Eng. A* **2019**, *751*, 183–190. [CrossRef]
24. Barkia, B.; Aubry, P.; Haghi-Ashtiani, P.; Auger, T.; Gosmain, L.; Schuster, F.; Maskrot, H. On the origin of the high tensile strength and ductility of additively manufactured 316L stainless steel: Multiscale investigation. *J. Mater. Sci. Technol.* **2019**, *41*, 209–218. [CrossRef]
25. Lei, J.; Xie, J.; Zhou, S.; Song, H.; Song, X.; Zhou, X. Comparative study on microstructure and corrosion performance of 316 stainless steel prepared by laser melting deposition with ring-shaped beam and Gaussian beam. *Opt. Laser Technol.* **2019**, *111*, 271–283. [CrossRef]
26. Hejripour, F.; Binesh, F.; Hebel, M.; Aidun, D.K. Thermal modeling and characterization of wire arc additive manufactured duplex stainless steel. *J. Mater. Process. Technol.* **2019**, *272*, 58–71. [CrossRef]
27. Stützer, J.; Totzauer, T.; Wittig, B.; Zinke, M.; Jüttner, S. GMAW Cold Wire Technology for Adjusting the Ferrite–Austenite Ratio of Wire and Arc Additive Manufactured Duplex Stainless Steel Components. *Metals* **2019**, *9*, 564. [CrossRef]
28. Zhang, X.; Wang, K.; Zhou, Q.; Ding, J.; Ganguly, S.; Marzio, G.; Yang, D.; Xu, X.; Dirisu, P.; Williams, S.W. Microstructure and mechanical properties of TOP-TIG-wire and arc additive manufactured super duplex stainless steel (ER2594). *Mater. Sci. Eng. A* **2019**, *762*, 138097. [CrossRef]
29. Ferro, P.; Bonollo, F. A Semiempirical Model for Sigma-Phase Precipitation in Duplex and Superduplex Stainless Steels. *Metall. Mater. Trans. A* **2012**, *43*, 1109–1116. [CrossRef]
30. Escriba, D.M.; Materna-Morris, E.; Plaut, R.L.; Padilha, A.F. Chi-phase precipitation in a duplex stainless steel. *Mater. Charact.* **2009**, *60*, 1214–1219. [CrossRef]
31. Llorca-Isern, N.; López-Luque, H.; López-Jiménez, I.; Biezma, M.V. Identification of sigma and chi phases in duplex stainless steels. *Mater. Charact.* **2016**, *112*, 20–29. [CrossRef]

32. Pohl, M.; Storz, O.; Glogowski, T. Effect of intermetallic precipitations on the properties of duplex stainless steel. *Mater. Charact.* **2007**, *58*, 65–71. [CrossRef]
33. Pardal, J.M.; Tavares, S.S.M.; Fonseca, M.C.; de Souza, J.A.; Côrte, R.R.A.; de Abreu, H.F.G. Influence of the grain size on deleterious phase precipitation in superduplex stainless steel UNS S32750. *Mater. Charact.* **2009**, *60*, 165–172. [CrossRef]
34. *ISO 14175: Welding Consumables—Gases and Gas Mixtures for Fusion Welding and Allied Processes*; ISO: Geneva, Switzerland, 2008.
35. Wallin, K.; Karjalainen-Roikonen, P.; Suikkanen, P. Sub-sized CVN specimen conversion methodology. *Procedia Struct. Integr.* **2016**, *2*, 3735–3742. [CrossRef]
36. *DNVGL-OS-F101: Submarine Pipeline Systems*; Det Norske Veritas AS: Høvik, Norway, 2012.
37. *ISO 9042: Steels—Manual Point Counting Method for Statistically Estimating the Volume Fraction of a Constituent with a Point Grid*; International Organization for Standardization: Geneva, Switzerland, 1998; p. 4.
38. *ISO 15156-1: Petroleum and Natural Gas Industries—Materials for Use in H2S-Containing Environments in Oil and Gas Production—Part 1: General Principles for Selection of Cracking-Resistant Materials*; ISO: Geneva, Switzerland, 2015.
39. *ISO 15156-3: Petroleum and Natural Gas Industries—Materials for Use in H2S-Containing Environments in Oil and Gas Production—Part 3: Cracking-Resistant CRAs (Corrosion-Resistant alloys) and Other Alloys*; ISO: Geneva, Switzerland, 2015.
40. *DNV Offshore Standard DNVGL-OS-C401: Fabrication and Testing of Offshore Structures*; Det Norske Veritas AS: Høvik, Norway, 2015.
41. Wu, C.; Li, S.; Zhang, C.; Wang, X. Microstructural evolution in 316LN austenitic stainless steel during solidification process under different cooling rates. *J. Mater. Sci.* **2016**, *51*, 2529–2539. [CrossRef]
42. Takalo, T.; Suutala, N.; Moisio, T. Austenitic solidification mode in austenitic stainless steel welds. *Metall. Trans. A* **1979**, *10*, 1173–1181. [CrossRef]
43. Hunter, A.; Ferry, M. Phase formation during solidification of AISI 304 austenitic stainless steel. *Scr. Mater.* **2002**, *46*, 253–258. [CrossRef]
44. Hammar, O.; Svensson, U. *Solidification and Casting of Metals: Proceedings of an International Conference on Solidification*; The Metals Society: London, UK, 1979.
45. Suutala, N. Effect of solidification conditions on the solidification mode in austenitic stainless steels. *Metall. Trans. A* **1983**, *14*, 191–197. [CrossRef]
46. Kotecki, D.J.; Siewert, T.A. WRC-1992 Constitution Diagram for Stainless Steel Weld Metals: A Modification of the WRC-1988 Diagram. *Weld. J.* **1992**, *71*, 171–178.
47. Liljas, M. The Welding Metallurgy of Duplex Stainless Steels. In Proceedings of the 4th International Conference, Welding Processes, Glasgow, Scotland, 13–16 November 1994; pp. 13–16.
48. Palmer, T.A.; Elmer, J.W.; Babu, S.S. Observations of ferrite/austenite transformations in the heat affected zone of 2205 duplex stainless steel spot welds using time resolved X-ray diffraction. *Mater. Sci. Eng. A* **2004**, *374*, 307–321. [CrossRef]
49. Park, S.; Shin, B.; Park, J.; Kim, D.; Chung, W. Effect of Austenite Morphology on the Electrochemical Properties of Super Duplex Stainless UNS S 32750. *Int. J. Electrochem. Sci.* **2019**, *14*, 5386–5395. [CrossRef]
50. Karlsson, L. Welding Duplex Stainless Steels—A Review Of Current Recommendations. *Weld. World* **2012**, *56*, 65–76. [CrossRef]
51. Nilsson, J.O.; Karlsson, L.; Andersson, J.O. Secondary austenite for mation and its relation to pitting corrosion in duplex stainless steel weld metal. *Mater. Sci. Technol.* **1995**, *11*, 276–283. [CrossRef]
52. Yang, J.; Wang, Q.; Wei, Z.; Guan, K. Weld failure analysis of 2205 duplex stainless steel nozzle. *Case Stud. Eng. Fail. Anal.* **2014**, *2*, 69–75. [CrossRef]
53. Pettersson, N.; Pettersson, R.F.A.; Wessman, S. Precipitation of Chromium Nitrides in the Super Duplex Stainless Steel 2507. *Metall. Mater. Trans. A* **2015**, *46*, 1062–1072. [CrossRef]
54. Liao, J. Nitride Precipitation in Weld HAZs of a Duplex Stainless Steel. *ISIJ Int.* **2001**, *41*, 460–467. [CrossRef]
55. Hertzman, S.; Pettersson, R.J.; Blom, R.; Kivineva, E.; Eriksson, J. Influence of Shielding Gas Composition and Welding Parameters on the N-content and Corrosion Properties of Welds in N-alloyed Stainless Steel Grades. *ISIJ Int.* **1996**, *36*, 968–976. [CrossRef]
56. Chen, T.H.; Yang, J.R. Microstructural characterization of simulated heat affected zone in a nitrogen-containing 2205 duplex stainless steel. *Mater. Sci. Eng. A* **2002**, *338*, 166–181. [CrossRef]

57. Hereñú, S.; Moscato, M.G.; Alvarez, I.; Armas, A.F. The Influence of Chromium Nitrides Precipitation on the Fatigue Behavior of Duplex Stainless Steels. *Procedia Eng.* **2014**, *74*, 179–182. [CrossRef]
58. Pettersson, R.F.A.; Hertzman, S.; Szakalos, P.; Ferreira, P.J. The Influence of Microstructure on Pitting Corrosion in Autogenous TlG Duplex Stainless Steel Welds. In Proceedings of the 4th International Conference, Welding Processes, Glasgow, Scotland, 13–16 November 1994.
59. Muthupandi, V.; Bala Srinivasan, P.; Seshadri, S.K.; Sundaresan, S. Effect of weld metal chemistry and heat input on the structure and properties of duplex stainless steel welds. *Mater. Sci. Eng. A* **2003**, *358*, 9–16. [CrossRef]
60. Atamert, S.; King, J.E. Intragranular nucleation of austenite. *Z. Fuer Met.* **1991**, *82*, 230–239.
61. Ramirez, A.J.; Lippold, J.C.; Brandi, S.D. The relationship between chromium nitride and secondary austenite precipitation in duplex stainless steels. *Metall. Mater. Trans. A* **2003**, *34*, 1575–1597. [CrossRef]
62. Lippold, J.C.; Al-Rumaih, A.M. Toughness and Pitting Corrosion of Duplex Stainless Steel Weld Heat-Affected Zone Microstructures Containing Secondary Austenite. In Proceedings of the 5th World Conference, Duplex Stainless Steels, Maastricht, The Netherlands, 21–23 October 1997; pp. 1005–1010.
63. Garzón, C.M.; Ramirez, A.J. Growth kinetics of secondary austenite in the welding microstructure of a UNS S32304 duplex stainless steel. *Acta Mater.* **2006**, *54*, 3321–3331. [CrossRef]
64. Nilsson, J.O. Super duplex stainless steels. *Mater. Sci. Technol.* **1992**, *8*, 685–700. [CrossRef]
65. Karlsson, L. Intermetallic Phase Precipitation in Duplex Stainless Steels and Weld Metals: Metallurgy, Influence on Properties and Testing Aspects. *Weld. World* **1999**, *43*, 20–41.
66. Nilsson, J.-O.; Huhtala, T.; Jonsson, P.; Karlsson, L.; Wilson, A. Structural stability of super duplex stainless weld metals and its dependence on tungsten and copper. *Metall. Mater. Trans. A* **1996**, *27*, 2196–2208. [CrossRef]
67. Atamert, S.; King, J.E. Sigma-phase formation and its prevention in duplex stainless steels. *J. Mater. Sci. Lett.* **1993**, *12*, 1144–1147. [CrossRef]